NANO · MICRO small
www.small-journal.com

Boosting Perovskite Photodetector Performance in NIR Using Plasmonic Bowtie Nanoantenna Arrays

Bin Wang, Yuting Zou, Huanyu Lu, Wenchi Kong, Subhash C. Singh, Chen Zhao, Chaonan Yao, Jun Xing, Xin Zheng, Zhi Yu, Cunzhu Tong, Wei Xin, Weili Yu,* Bo Zhao, and Chunlei Guo**

Triple-cation mixed metal halide perovskites are important optoelectronic materials due to their high photon to electron conversion efficiency, low exciton binding energy, and good thermal stability. However, the perovskites have low photon to electron conversion efficiency in near-infrared (NIR) due to their weak intrinsic absorption at longer wavelength, especially near the band edge and over the bandgap wavelength. A plasmonic functionalized perovskite photodetector (PD) is designed and fabricated in this study, in which the perovskite ($(Cs_{0.06}FA_{0.79}MA_{0.15})Pb(I_{0.85}Br_{0.15})_3$) active materials are spin-coated on the surface of Au bowtie nanoantenna (BNA) arrays substrate. Under 785 nm laser illumination, near the bandedge of perovskite, the fabricated BNA-based plasmonic PD exhibits ≈2962% enhancement in the photoresponse over the Si/SiO_2-based normal PD. Moreover, the detectivity of the plasmonic PD has a value of 1.5×10^{12} with external quantum efficiency as high as 188.8%, more than 30 times over the normal PD. The strong boosting in the plasmonic PD performance is attributed to the enhanced electric field around BNA arrays through the coupling of localized surface plasmon resonance. The demonstrated BNA-perovskite design can also be used to enhance performance of other optoelectronic devices, and the concept can be extended to other spectral regions with different active materials.

1. Introduction

In recent years, metal halide perovskites have attracted enormous research attention as light absorbers for a range of optoelectronic applications owing to their facile solution processing ability, large light absorption coefficient, long carrier diffusion length, low exciton binding energy, and high carrier mobility.[1–7] The excellent bandgap tunability through engineering their chemical composition makes them ideal candidates for optoelectronic devices such as light-emitting diodes, solar cells, and photodetectors with large power conversion efficiency.[8–12] The triple-cation mixed metal halide perovskite ($(Cs_{0.06}FA_{0.79}MA_{0.15})Pb(I_{0.85}Br_{0.15})_3$) with high external quantum yields of 66% (translate to internal yields that exceed 95%) has proven its application in solar cells with a conversion efficiency as high as 21.7%.[13] Moreover, higher thermal stability, less susceptible to moisture, and higher fabrication tolerance of $(Cs_{0.06}FA_{0.79}MA_{0.15})Pb(I_{0.85}Br_{0.15})_3$ perovskite over a typical lead halide perovskites, e.g., $MAPbI_3$ and $FAPbI_3$, make it an ideal candidate for environmentally robust and highly efficient optoelectronic devices.[14,15] However, the weak intrinsic absorption of perovskites in near infrared (NIR) leads to a rapid decrease in the photocurrent of perovskite-based photodetector (PD), which limits its application in broadband photodetection at NIR and longer wavelengths.[16–18] To improve the photoresponse of perovskite-based PDs in the NIR, various materials and chemical doping strategies have been explored.[19–21] However, the performance of perovskite-based PDs in the NIR range is still limited.

Dr. B. Wang, Dr. Y. Zou, Dr. W. Kong, Dr. S. C. Singh, Dr. C. Zhao, Dr. C. Yao, Dr. J. Xing, Dr. X. Zheng, Dr. Z. Yu, Dr. W. Xin, Prof. W. Yu, Dr. B. Zhao, Prof. C. Guo
The Guo Photonics Laboratory
State Key Laboratory of Applied Optics
Changchun Institute of Optics
Fine Mechanics and Physics
Chinese Academy of Sciences
Changchun 130033, P. R. China
E-mail: ssingh49@ur.rochester.edu; weili.yu@ciomp.ac.cn; guo@optics.rochester.edu

The ORCID identification number(s) for the author(s) of this article can be found under https://doi.org/10.1002/smll.202001417.

DOI: 10.1002/smll.202001417

Dr. B. Wang, Dr. Y. Zou, Dr. H. Lu, Dr. W. Kong, Dr. C. Zhao, Dr. C. Yao, Dr. J. Xing, Dr. X. Zheng
University of Chinese Academy of Sciences
Beijing 100049, P. R. China

Dr. H. Lu, Prof. C. Tong
State Key Laboratory of Luminescence and Applications
Changchun Institute of Optics
Fine Mechanics and Physics
Chinese Academy of Sciences
Changchun 130033, P. R. China

Dr. S. C. Singh, Prof. C. Guo
The Institute of Optics
University of Rochester
Rochester, NY 14627, USA

Plasmonic effect utilizes metal nanoparticles or engineered metal nanostructures to confine light from free space into sub-wavelength dimension with strong electric field (E-field) enhancement due to the coupling of localized surface plasmon resonance (LSPR) of metallic nanostructures with incident light field.[22–26] The plasmonic effect is one of the prominent approaches to improve the photovoltaic performances of PDs,[27–30] solar cells,[31–34] and plasmonic sensors[35,36] though the mechanism of far-field scattering, near-field enhancement, and charge carrier or resonant energy transfer.[37] For instance, the triangular shape of bowtie nanoantennas (BNAs) has been used for efficient resonant plasmonic coupling between the triangle tips resulting in a strong localized E-field enhancement in the nanogap.[38–40] The inherent advantages of strong E-field enhancement enabled BNA applications in a number of plasmonic and optoelectronic devices, including optical sensing, nanoscale light sources, and photoelectric devices.[41–44] Besides the extraordinary strong E-field enhancement, the BNAs have also shown other functionalities such as better directionality, higher tunable broadband spectral response, better electrooptical driving, and polarization control over other coupled dipole antenna designs.[45–47] Recently, the out-of-plane near-field coupling between metallic nanoparticles and a metallic thin film separated by a dielectric spacer, known as the metal–insulator–metal (MIM) structure, has been studied intensely to further enhance the localized E-field.[48] An intelligent design of a plasmonic BNA system to enhance photon absorption coefficient near the band edge or over the bandgap wavelength of perovskite can significantly boost the NIR performance and operation bandwidth of perovskite-based PDs.

In this study, we demonstrated a significant improvement in the performance of a triple-cation mixed metal halide perovskite-based ($(Cs_{0.06}FA_{0.79}MA_{0.15})Pb(I_{0.85}Br_{0.15})_3$) PD in NIR utilizing a plasmonic-functionalized substrate consisting of Au BNA arrays on an Au thin film separated by a SiO_2 spacer layer (BNA arrays/spacer layer/Au film, MIM configuration). Compared to the perovskite PD on a typical Si/SiO_2 substrate (Si/SiO_2-based normal PD), the responsivity of perovskite PD fabricated on a plasmonic BNA array substrate (BNA-based plasmonic PD) exhibited a giant enhancement factor (EF) of 2962% under 785 nm light illumination. The strong boosting in the plasmonic PD performance at 785 nm, near the band edge, is attributed to the enhanced E-field induced increase in the light absorption coefficient through the LSPR coupling of BNA arrays with the incident light field. The finite-difference time-domain (FDTD) simulations were performed to calculate the spectral E-field enhancement and spatial distribution of E-field around BNA arrays at the excitation wavelength. Under 785 nm laser illumination, the maximum value of D^* for the plasmonic PD is two orders of magnitude larger than the normal PD. Similarly, the external quantum efficiency (EQE) of plasmonic PD is ≈30 times larger as compared to the normal PD under 785 nm illumination. The plasmonic PD device has "ON" (τ_{on}) and "OFF" (τ_{off}) response times as low as 49 and 27 ms, respectively, demonstrating its high-frequency photoswitching capability. Through plasmonic integration, we brought NIR performance of perovskite PD comparable to the visible region (532 and 633 nm) even though the used perovskite material has comparatively negligible intrinsic absorption at operating wavelength in the NIR. The plasmonic PD also exhibits a high light on/off ratio of $>10^5$ and a stable photocurrent for over 30 d under 785 nm laser illumination. Our design shows that through introducing the plasmonic nanostructure, the perovskite PD can overcome the weak intrinsic absorption of perovskite at longer wavelength to boost its NIR performance to the level of its performance in the visible to increase its bandwidth of photodetection. The demonstrated BNA-perovskite design can also be used to improve performance of other optoelectronic devices, such as phototransistors, solar cells, and light-emitting diode and the concept can be extended to other spectral regions with different active materials and different geometric parameters of BNA arrays.

2. Results and Discussion

2.1. Plasmonic BNA Arrays Design and Theoretical Modeling

First, the plasmonic substrate for perovskite PD is theoretically designed, where arrays of Au BNA site on Ti/Au film separated by a SiO_2 thin layer as spacer, and Si/SiO_2 is selected as substrate, as shown in **Figure 1**a. In order to maximize the light–matter interaction of perovskite PD in NIR region, the periodic BNA arrays and MIM configuration are selected, which exploit the coordinated effects of multiple coupling to increase the broadband tunability in the spectral response and significantly enhanced electromagnetic field.[49,50] The theoretical design and modeling are performed using FDTD method by a commercial FDTD package known as Lumerical solutions (Lumerical Inc.). A 3D model is used to study the E-field EF calculated as $|E|^2/|E_0|^2$, where E_0 is the incident laser field and E is the resulting near field (Details can be seen in the Experimental Section, FDTD Simulations).

Guided by our previous work,[50,51] a sweeping over the domain of the design parameter, side length of BNA, was performed using FDTD simulation (Figure S1, Supporting Information). The optimal designed parameters included 400 nm of side length, 150 nm of gap distance, 110 nm of triangle thickness (10 nm Ti and 100 nm Au), 550 nm of transverse period, and 2 µm of vertical period (Figure 1a). 20 nm Ti and 50 nm Au films, deposited on Si/SiO_2 substrate (2 µm Si and 300 nm SiO_2), were used to totally block the light transmission through the structure. A 20 nm thin SiO_2 layer, separating BNA array with Au film, constituted the MIM configuration as a quasi "Fabry–Perot" cavity. Figure 1b presents the calculated E-field EF as a function of excitation wavelength at P_0 point in the center of BNA (inset image, x, $y = 0$, $z = 50$ nm) and shows a broadband enhancement of E-field from 600 to 1000 nm. The strong enhancement of E-field in the broadband spectral region can compensate the weak absorption of perovskite in NIR and potentially improve the photoresponse of perovskite PD. Especially the peak of E-field enhancement of designed plasmonic platform at 775 nm, close to the 785 nm of laser illumination wavelength in the measurement of perovskite PD, can improve light–matter interaction of perovskite at illumination wavelength to enhance its absorption and hence possibly PD responsivity. Figure 1c,e shows the E-field distribution ($|E|^2/|E_0|^2$) in x-y and x-z plane under 775 nm excitation. One can see that

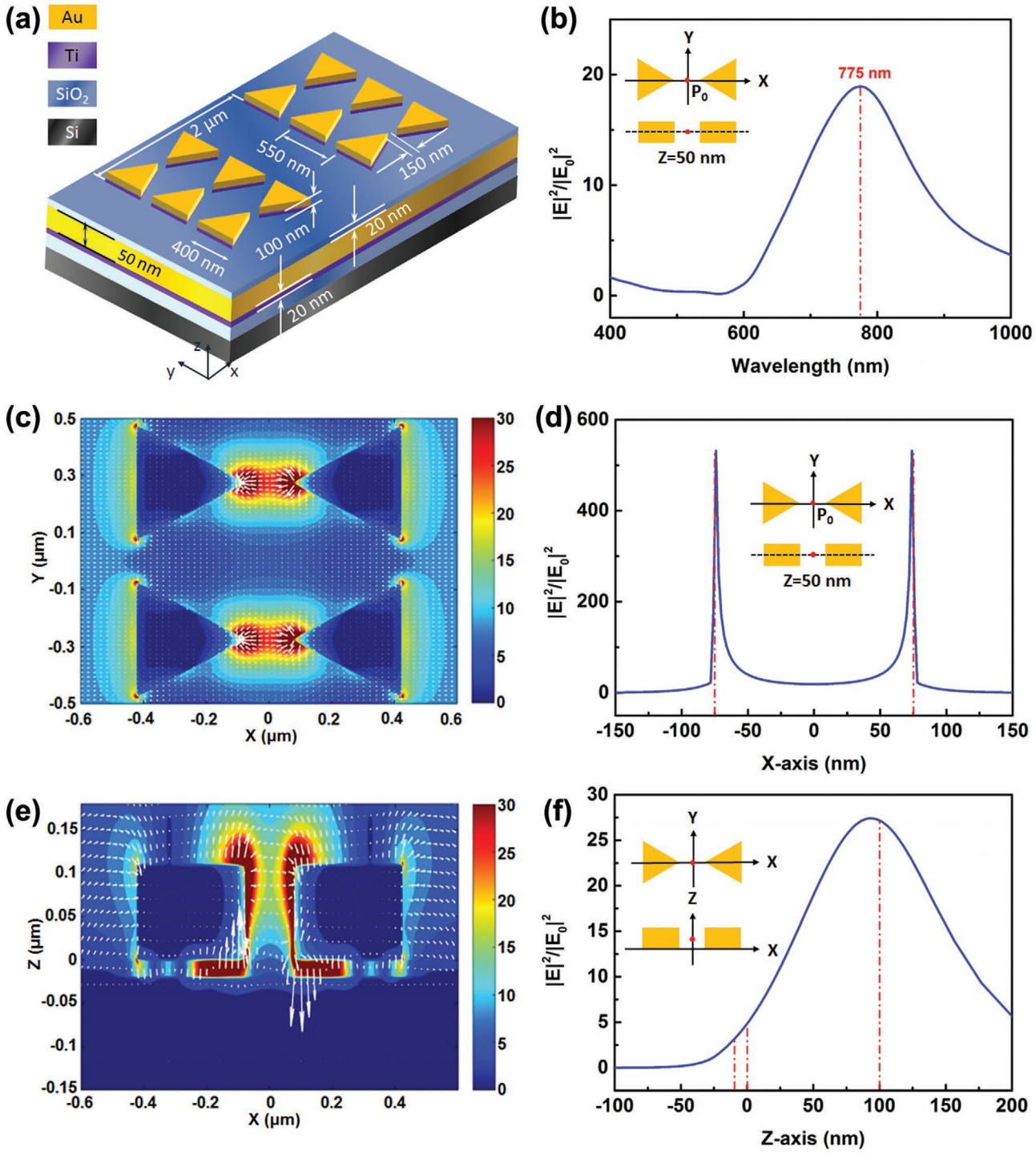

Figure 1. a) Designed geometrical parameters of BNA arrays with MIM configuration. b) Calculated E-field EF of BNA arrays with excitation wavelength at P_0 point (inset). c,e) The E-field distribution ($|E|^2/|E_0|^2$) under 775 nm (LSPR mode) in *x*-*y* and *x*-*z* plane. d,f) Spatial distribution ($|E|^2/|E_0|^2$) of E-field versus distance along *x*-axis and *z*-axis under 775 nm.

the E-field is primarily localized in the bowtie gap, which is caused by the coupling of dipolar LSPR mode between two closely spaced nanoprisms. In addition, the E-field also localized at the edges and outer corners with comparatively smaller intensity due to the coupling of higher order LSPR modes. Moreover, the enhanced E-field is also confined below both the tips and the ridges of the BNA due to mode coupling of the quasi "Fabry–Perot" cavity in MIM configuration. The spatial distribution ($|E|^2/|E_0|^2$) of E-field along *x*-axis and *z*-axis under 775 nm excitation are also shown in Figure 1d,f, respectively.

2.2. Characterization of Plasmonic BNA Arrays Substrate and Perovskite Film

Figure 2a shows the scanning electron microscopy (SEM) image of the top view of fabricated plasmonic BNA arrays with a magnified view of two pairs of Au BNA as an inset. It shows that the geometric parameters of fabricated BNA arrays, including side length of 400 ± 5 nm, gap distance of 150 ± 2 nm, transverse period of 545 ± 5 nm, and vertical period of 2 μm, are close to the theoretical design. The average *z*-height of BNA array is ≈104 ± 3 nm as measured using atomic force microscopy (AFM) (Figure S2, Supporting Information), which is also close to the theoretically optimized value. The optical absorption of BNA array and Si/SiO_2 substrate (300 nm SiO_2 on the top of Si wafer) in the visible–NIR spectral region (400–1000 nm) are shown in Figure 2b. In comparison with Si/SiO_2 substrate, the absorbance of BNA substrate is greatly enhanced, especially in the longer wavelength range from 600 to 1000 nm where perovskite has comparatively lower intrinsic absorption coefficient.

Figure 2c shows the SEM image of the spin-coated perovskite film ($(Cs_{0.06}FA_{0.79}MA_{0.15})Pb(I_{0.85}Br_{0.15})_3$) on Si/SiO_2 substrate with grain size in the range of hundred nanometers. The cross-sectional SEM image of perovskite film is displayed in Figure S2 (Supporting Information). The average thickness of perovskite film is around 150 nm. The powder X-ray diffraction (XRD) pattern shows strong diffraction peaks exhibiting the high crystalline quality of perovskite polycrystalline film (Figure S3a, Supporting Information). The XRD peaks with their respective crystal planes confirm the intrinsic phase of perovskite as previously reported.[13,14] Two extremely small peaks observed at 11.7° and 12.5° correspond to non-perovskite δ-phase $FAPbI_3$ and PbI_2, which would not affect the optical properties of the perovskite.[14,15] Moreover, the energy-dispersive X-ray spectroscopy (EDS) was carried out to determine the elemental contents of perovskite film (Figure S3b, Supporting Information). Color maps of every elemental EDS analysis of perovskite film are shown in Figure S4 (Supporting Information), which showed the uniformity of element distribution. A high-resolution X-ray photoelectron spectroscopy (XPS) measurement of perovskite film further demonstrates its structural purity and chemical composition (Figure S5, Supporting Information). The vis–NIR absorption spectrum of the perovskite film (Figure 2d) on the Si/SiO_2 substrate shows strong absorption in the visible, but a sudden drop in the absorbance after ≈750 nm. The absorption cutoff at ≈770 nm, corresponding to the band edge of the perovskite, demonstrates almost negligible intrinsic absorption in the NIR. The optical bandgap of perovskite is estimated from optical absorption spectrum following Tauc's equation

$$\left[F(R)*h\nu\right]^{1/2} = A\left(h\nu - E_g\right) \tag{1}$$

where $F(R)$ is the measured absorption coefficient, E_g is the bandgap width, and A is a constant depending on the transition probability. The linear intercept of the Tauc plot on x intercepts gives the optical bandgap of the $(Cs_{0.06}FA_{0.79}MA_{0.15})Pb(I_{0.85}Br_{0.15})_3$ perovskite as 1.61 eV (Figure 2d, inset).

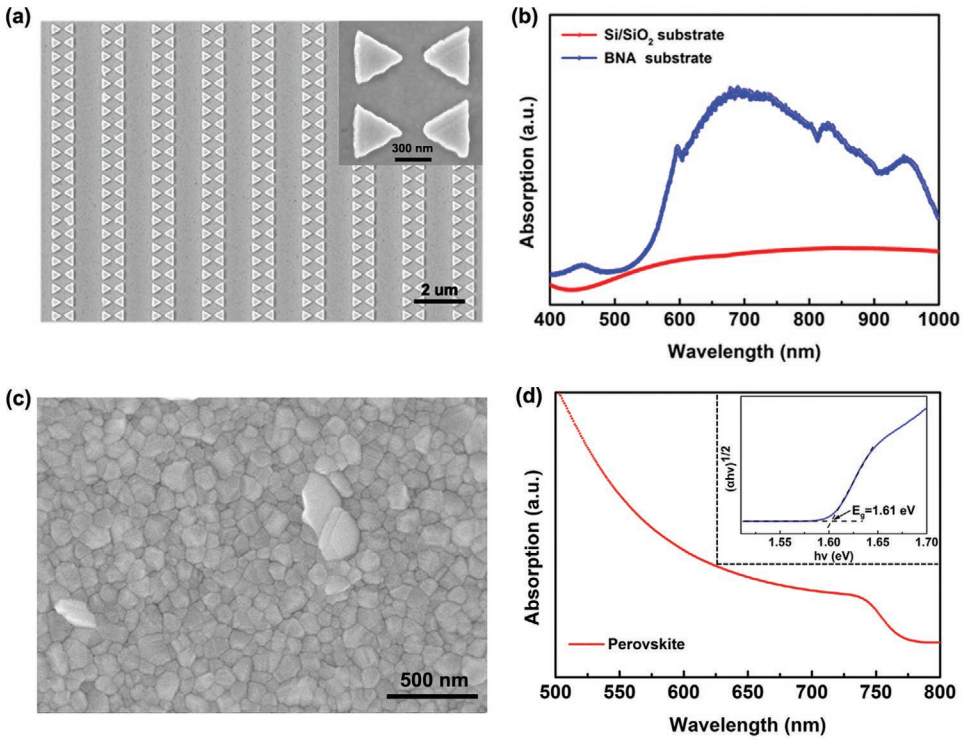

Figure 2. a) SEM image of top view of BNA arrays. b) Vis–NIR absorption spectra of BNA and Si/SiO_2 substrates. c) SEM image of perovskite film on Si/SiO_2 substrate. d) Vis–NIR absorption spectrum of perovskite film, inset shows calculated bandgap (1.61 eV) of perovskite.

2.3. Steady-State and Time-Resolved Photoluminescence of Plasmonic Perovskite PD

The schematic design of BNA-based plasmonic PD is illustrated in **Figure 3**a. In detail, a layer of perovskite film with an average thickness of 150 nm was spin-coated onto the plasmonic BNA array substrate followed by thermal evaporative deposition of 80 nm thick Au source/drain (S/D) electrodes. About 10 nm of thin SiO_2 insulating layer was deposited between perovskite and plasmonic substrate to suppress charge transfer, particularly electron leakage from bowtie tip to the perovskite at metal–perovskite interface, while still allowing the perovskite sensitizer to take the advantage of the plasmonic light trapping through enhanced E-field.[52,53] The schematic of fabrication process is shown in Figure S6 (Supporting Information, experimental fabrication see Section 4.2). Figure 3b,c shows the SEM images of perovskite film spin-coated onto the BNA array substrate at different magnifications, where vertical columns (Figure 3b) are arrays of Au BNA. The SEM images show that the spin-coated perovskite film completely covers the BNA arrays substrate without breaking the tight packing of grains of perovskite. In order to better understand the working mechanism of our PD device, the schematic of the band diagram of the device is displayed in Figure 3d. The energy levels for the conduction band (CB) and the valence band (VB) of perovskite are 3.84 and 5.43 eV, respectively.[54] The Fermi level (E_f) of Au is 5.1 eV. As shown in Figure 3d, the electric field gradient can facilitate the effective hole transfer from perovskite to the top Au electrodes. Due to the high work function of contacted Au electrodes, an ohmic contact is well formed at the interface between perovskite and Au electrode, which is experimentally confirmed in the next sections with *I–V* measurement.

Figure 3e,f presents the steady-state and time-resolved photoluminescence (PL) spectrum of BNA-based plasmonic PD (red curve) and Si/SiO_2-based normal PD (blue curve), respectively. The peak position of the emission is almost consistent in both PD devices (Figure 3e), which centers at 775 nm (1.6 eV) corresponds to the excitonic recombination across bandgap and supports our bandgap measurements (1.61 eV) using Tauc's plot (Figure 2d). However, the PL intensities of both devices are quite different. Compared to the case of normal PD, the PL intensity of the plasmonic PD shows a clear quenching and is approximately half value of the normal PD. The quenching in the steady-state PL is attributed to the reduced carrier recombination rate and enhanced charge separation, which is related to the electrostatic potential at the plasmonic-BNA/perovskite interface and plasmonic effect of BNA arrays.[55–57] Then, the time-resolved PL spectrums for plasmonic and normal PDs are measured as shown in Figure 3f. The PL decay dynamics are well fitted using a biexponential decay

$$Fit = A + B_1 e^{(-t/\tau_1)} + B_2 e^{(-t/\tau_2)} \quad (2)$$

where A, B_1, and B_2 are constants, t is the time, while τ_1 and τ_2 are the time constants for radiative and nonradiative recombination, respectively.[58] By fitting, an obvious shorter PL lifetime of 4.64 ns, measured for the perovskite film on plasmonic BNA substrate, is observed, as compared to that of perovskite

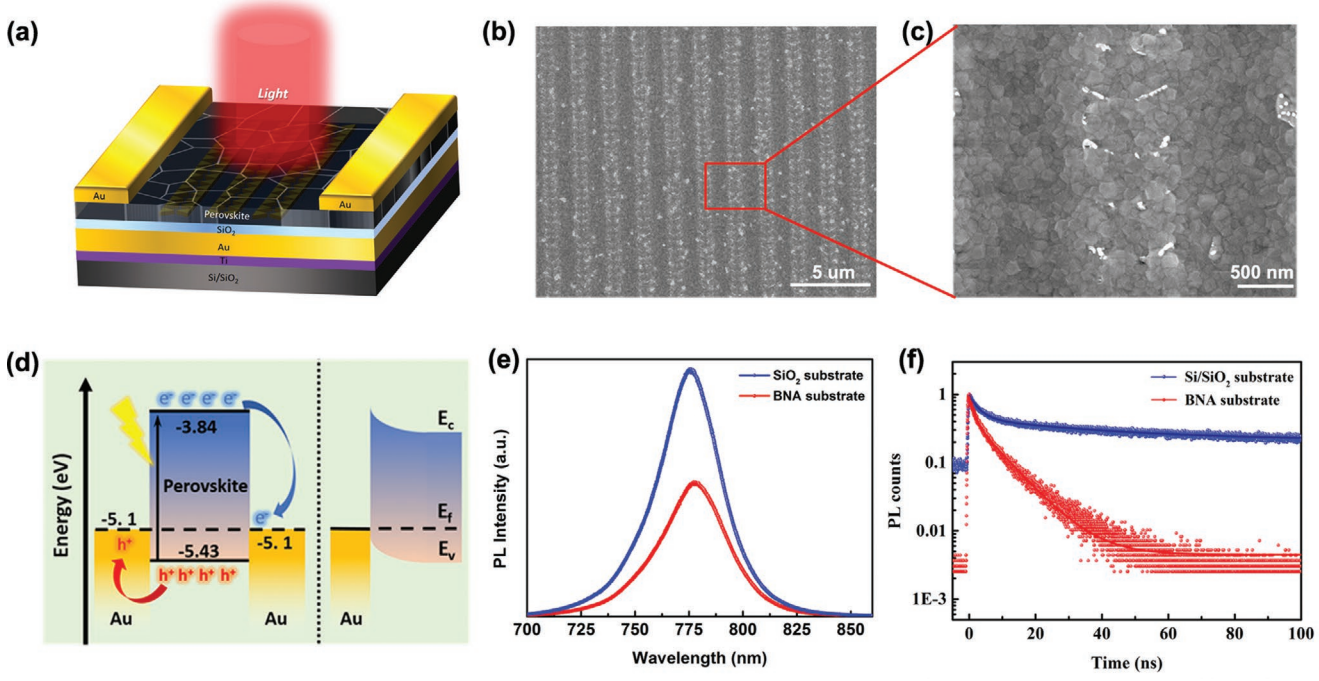

Figure 3. a) Schematic of BNA-based plasmonic PD. b,c) SEM image of the spin-coated perovskite film on plasmonic substrate at different magnifications (scale bars: 5 µm and 500 nm). d) The energy level diagram of the perovskite PD. e,f) The steady-state PL (473 nm excitation) spectrum and time-resolved PL decay traces (478 nm excitation) of Si/SiO_2-based normal PD (blue curve) and BNA-based plasmonic PD (red curve), respectively. All the comparison of the steady-state and time-resolved PL measurements are done under the same experimental conditions.

film on the normal Si/SiO_2 substrate (14.58 ns). The enhanced quenching of PL lifetime, followed the trend of steady-state PL, indicates an enhanced excitons separation, improved charge diffusion, and reduced carrier accumulation and recombination in the plasmonic-BNA/perovskite system, which will result in an efficient carrier extraction to the collectors and thus prospectively improve the performance of the plasmonic perovskite PD.[59–62] The PL mappings for plasmonic and normal PDs illustrate the uniformity of the perovskite film and difference in PL intensity in two PD systems (Figure S7, Supporting Information).

2.4. Photoelectric Performance Characterization of Plasmonic Perovskite PD

To study the plasmonic effect of BNA arrays on the optoelectronic performance of perovskite PD, we measured the current–voltage (*I–V*) characteristics of the BNA-based plasmonic PD under different wavelengths and intensities of laser illumination, and compared its performance with Si/SiO_2-based normal PD. **Figure 4**a shows the *I–V* curves for dark and under 785 nm laser illumination (110.17 mW cm^{-2}) for the plasmonic and normal PD. The typical ohmic nature of *I–V* curves demonstrates formation of good ohmic contacts between perovskite active material and Au S/D electrodes. At a bias voltage of 5 V, the photocurrent from plasmonic PD is 2.58 μA resulting in ≈29 times enhancement as compared to normal PD (0.09 μA). The plasmonic EF is defined as follows

$$\mathrm{EF} = \frac{I_{p2} - I_{p1}}{I_{p1}}(\%) \tag{3}$$

where I_{p2} and I_{p1} are photocurrents for plasmonic and normal PDs, respectively. The EF for plasmonic PD is ≈2767% over the normal PD. Moreover, a large value of photocurrent (I_p: 2.58 μA) from plasmonic PD over its dark current (I_d: 1.2×10^{-5} μA) demonstrates its high signal-to-background ratio. Thus, a large value, 2.15×10^5, of light on/off ratio (I_p/I_d) indicates a high-quality photosensitive switching characteristic of plasmonic PD. The *I–V* logarithm curves of plasmonic and normal PDs under 785 nm laser illumination with different illumination intensities are shown in Figure S8a,b (Supporting Information). The values of photocurrent increase with increasing illumination intensities for both types of PDs due to the fact that the photogenerated charge carrier density is proportional to the absorbed photon flux. However, for a given laser intensity, photocurrent from the plasmonic PD is one to two orders (10 to 100 times) of magnitude higher than the normal PD. It is worth mentioning that the bandgap, 1.61 eV, of the perovskite ($(Cs_{0.06}FA_{0.79}MA_{0.15})Pb(I_{0.85}Br_{0.15})_3$) used in the PDs is (Figure 2d, inset) larger than the energy of incident photons at 785 nm leading to a weak intrinsic photon absorption and proportionally a low photocurrent. However, by using the BNA arrays substrate, the photoelectric conversion efficiency of plasmonic PD is tremendously improved under 785 nm laser illumination.

Based on the measured photocurrents and the incident laser power densities, the responsivity of the PD is calculated as follows[63]

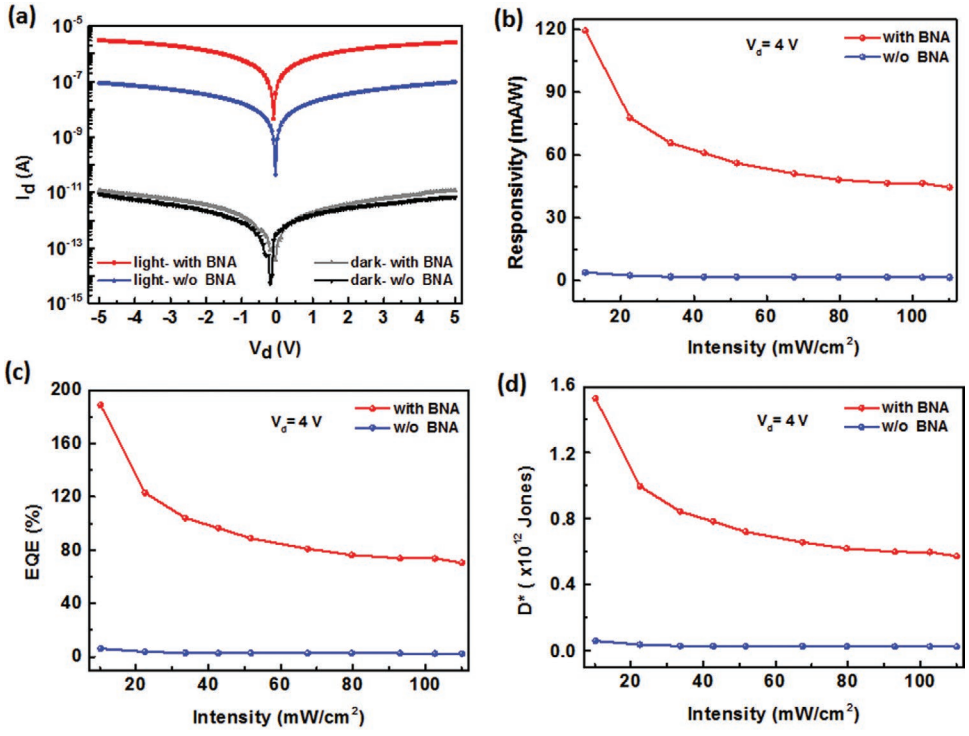

Figure 4. a) *I–V* characteristics of plasmonic (with BNA) and normal (w/o BNA) PDs under laser illumination (110.17 mW cm^{-2}) and dark. b–d) The responsivity, EQE, and *D** of plasmonic (with BNA) and normal (w/o BNA) PDs as a function of laser illumination intensity at bias voltages of 4 V, respectively. Notice, all the measurement and calculation are under 785 nm laser illumination.

$$R = \frac{\left(I_p - I_d\right)}{P_{opt} \cdot S} \quad (4)$$

where R is responsivity, I_p is the photocurrent, I_d is the dark current, P_{opt} is the incident laser power density, and S is the effective working area of the device. The relationship between the responsivity and the applied bias voltage for plasmonic and normal PDs under different illumination intensities is shown in Figure S8c,d (Supporting Information). The responsivity of both perovskite PDs increases almost linearly with the applied bias voltage in the studied voltage range of 0–4 V (Figure 4b). For a given illumination intensity of 10.17 mW cm^{-2} (785 nm), the responsivities of the plasmonic and normal PDs have maximum values of 119.4 and 3.9 mA W^{-1} exhibiting an EF of ≈2962%. The higher plasmonic EF in the responsivity at lower illumination intensities shows its excellent performance in the detection of low photon density. For a high illumination intensity of 100 mW cm^{-2} and above, the responsivity of the plasmonic PD attains a constant value 46 mA W^{-1}, which is ≈31 times larger than the corresponding value of 1.5 mA W^{-1} for the normal PD.

The EQE of the PDs is calculated using measured photocurrents and incident laser power densities as follows[64]

$$\mathrm{EQE} = \frac{I_p/q}{P_{opt}/h\nu} = R\frac{hc}{\lambda q} \quad (5)$$

where h and c are the Planck's constant and speed of light, λ is the wavelength of laser illumination, R is responsivity, and q is elementary charge. As shown in Figure 4c, the EQE of plasmonic PD has a maximum value of 188.8% which is ≈30 times larger than the corresponding EQE value (6.2%) of the normal PD. The variations in EQE with bias voltage at different laser illumination intensities for plasmonic and normal PDs are shown in Figure S8g,h (Supporting Information). The EQE shows almost linear increase with the bias voltage due to the fast collection rate of photogenerated charge carrier from the active region by the S/D electrodes.[29]

We further evaluated the specific detectivity (D^*), which is another key parameter to determine the performance metrics of photodetectors. There are three factors contributing to the noise that limits D^*, namely: i) shot noise from the dark current, ii) Johnson noise, and iii) thermal fluctuation or "flicker" noise. In the present case, the shot noise from the dark current (J_d) is the major contributor to the overall photodetector noise.[65–67] Therefore, D^* can be expressed according to the following expression

$$D^* = \frac{R}{\sqrt{2qJ_d}} = \frac{\sqrt{S}\cdot R}{\sqrt{2qI_d}} \quad (6)$$

where I_d is the dark current, R is the responsivity, q is elementary charge, and S is the effective working area of the device. Figure 4d shows variations in the D^* with the incident laser intensity for plasmonic and normal PDs. One can see that the value of D^* for plasmonic PD decreases with an increase in the incident illumination intensity and has a maximum value of 1.5×10^{12} Jones (1 Jones = 1 cm Hz$^{1/2}$ W^{-1}) at the minimum illumination intensity (10.17 mW cm^{-2}) used in the present study. As compared to the normal PD (5.8×10^{10} Jones), the plasmonic PD shows ≈30 times improvement in the value of D^*. The value of D^* reflects the capability of a PD device to detect a weak light signal, and a high D^* value of our plasmonic PD demonstrates its potential application in the weak near-infrared light sensing and imaging. The variations in the D^* with the applied bias voltage for plasmonic and normal PDs under different incident illumination intensities are shown in Figure S8e,f (Supporting Information).

In order to demonstrate the role of the plasmonic BNA array on the improved performance of perovskite PD, we further studied the optoelectronic properties of plasmonic perovskite PD under 633 and 532 nm laser illuminations. **Figure 5**a–d shows the optoelectronic characteristic curves of plasmonic and normal PD under 633 nm laser illumination. The I–V logarithm curves for both types of PDs, measured in the dark and under laser illumination (λ = 633 nm, 11.04 mV cm^{-2}), are shown in Figure 5a. At a given bias voltage of 5 V, the photocurrent increases from 0.11 μA in the normal PD to 0.2 μA in the plasmonic PD with EF of 81.8%. Similar to the NIR laser illumination (785 nm), the responsivity of both PDs also decreases with an increase in the illumination intensity in the visible range (Figure 5b for 633 nm, and Figure 5f for 532 nm). For a minimum illumination intensity of 1.68 mW cm^{-2} under 633 nm (4 V of bias voltage), the responsivity of the plasmonic PD has a value of 122.5 mA W^{-1} which is 93.5% higher over the normal PD (63.3 mA W^{-1}). Furthermore, the variations in the EQE and D^* of both PDs with the incident illumination intensity are shown in Figure 5c,d, respectively. Under 633 nm laser illumination, one can see that both EQE and D^* decrease with an increased illumination intensity, and have the maximum values of 285.9% and 1.57×10^{12} Jones for plasmonic PD as compared to 47.6% and 1.01×10^{12} Jones for normal PD. For 532 nm laser illumination, the optoelectronic performances of plasmonic and normal perovskite PD are shown in Figure 5e–h. The maximum photocurrent increases from 0.55 μA in the normal PD to 0.87 μA in the plasmonic PD with EF of 58.2%. The responsivity has maximum values of 192.5 and 150.5 mA W^{-1} for the plasmonic and normal PDs, respectively, under a laser illumination intensity of 2.61 mW cm^{-2}. The maximum values of EQE and D^* are estimated to be 449.2% and 2.47×10^{12} Jones, respectively, for the plasmonic PD and 351.2% and 2.40×10^{12} Jones for the normal PD, respectively. From these measurements (Figure 5e–h), we can see that there is a negligible plasmonic enhancement under 532 nm laser illumination over the 785 nm irradiation. The variations in I–V, responsivity, EQE, and D^* with bias voltages for the plasmonic and normal PDs under different laser illumination intensity at 633 and 532 nm are shown in Figures S9 and S10 (Supporting Information), respectively.

2.5. Mechanism for the Improvement of PD Performance Using Plasmonic BNA Arrays

As discussed in the previous section, the performance of the plasmonic PD has dramatically improved under 785 nm laser illumination. However, it demonstrated comparatively lower improvement under 633 nm and almost negligible

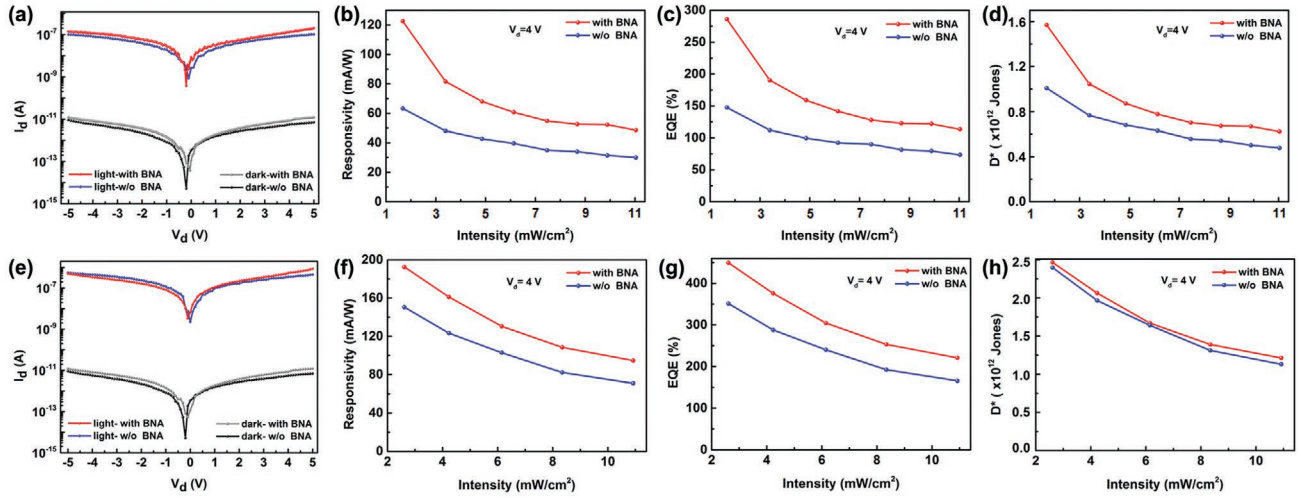

Figure 5. a,e) *I–V* characteristics of the plasmonic (with BNA) and normal (w/o BNA) PDs under 633 nm (11.04 mV cm^{-2}) and 532 nm (10.92 mV cm^{-2}) laser illumination, respectively. b–d) The responsivity, EQE, and *D** of the plasmonic (with BNA) and normal (w/o BNA) PDs as a function of laser illumination intensity (λ = 633 nm) at bias voltages of 4 V, respectively. f–h) The responsivity, EQE, and *D** of the plasmonic (with BNA) and normal (w/o BNA) PDs as a function of laser illumination intensity (λ = 532 nm) at bias voltages of 4 V, respectively.

enhancement under 532 nm laser illuminations. To understand the wavelength dependent enhancement mechanism in more detail, we simulated the E-field distribution of BNA arrays at 785, 633, and 532 nm wavelengths, as shown in **Figure 6**a–c ($|E_z|$ distribution at different wavelengths see Figure S11, Supporting Information). Figure 6a shows strong enhancement in the localized E-field in the gap of BNA arrays under 785 nm excitation, close to the LSPR peak of BNA at 775 nm (Figure 1b), where the perovskite has a weak intrinsic absorption (Figure 2d). Therefore, the dramatic boosting in the photoelectric performance of the plasmonic PD under 785 nm irradiation is mainly due to the enhanced E-field induced increase in the light absorption coefficient, instead of the weak intrinsic absorption of perovskite, through the LSPR coupling of BNA arrays with the incident light field.[28,29] At 532 nm laser illumination, the perovskite has several times higher intrinsic absorption as compared to 633 and 785 nm (Figure 2d). However, as shown in Figure 6c, the localized E-field has almost negligible enhancement at 532 nm wavelength resulting in a negligible enhancement in the photoelectric performance of plasmonic PD. Therefore, the large but almost similar photoelectric performance of both PDs under 532 nm laser illumination is the result of larger intrinsic absorption of the perovskite at 532 nm wavelength, instead of weakest E-field enhancement of BNA arrays. For 633 nm laser illumination, the intrinsic absorption of the perovskite is in between 532 and 785 nm (Figure 2d) and the localized E-field has a lower enhancement distributed around tips of BNA (Figure 6b). The overall photoelectric performance of plasmonic PD under 633 nm laser illumination is the combination of intrinsic absorption of perovskite and E-field enhancement of BNA arrays, however the photoelectric performance of plasmonic PD is still lower compared with 532 and 785 nm. The reason is that the lower enhanced E-field at 633 nm is less enough to compensate for the difference of intrinsic absorption between 532 and 633 nm, leads to the weaker photoelectric performance compared with 532 nm. But for 785 nm, the extremely enhanced E-field can not only compensate for the difference of intrinsic absorption between 785 and 633 nm, but also make the photoelectric performance comparable to 532 nm. We can conclude that the hugely enhanced E-field by plasmonic BNA arrays is responsible for a large improvement in the performance of perovskite PD in NIR spectral range. The plasmonic improvement in the photoelectric performance of plasmonic PD over normal one is proportional to the E-field enhancement near the BNA arrays.

In order to exhibit the wavelength-dependent enhancement phenomenon more intuitively, we compared the variations in responsivity, *D**, and EQE of plasmonic and normal PDs under 532, 633, and 785nm laser illuminations at the same intensity of 11 mW cm^{-2}, as shown in Figure 6d–f. As shown in Figure 6d, the responsivity of both PDs increases almost linearly with an increase in the applied bias voltage for 532 (green curve), 633 (blue curve), and 785 nm (red curve) laser illumination. As discussed above, the normal PD shows the lowest responsivity under 785 nm laser illumination as compared to all other illumination wavelengths which is due to the low intrinsic absorption of the perovskite at 785 nm wavelength. However, for the plasmonic PD, the responsivity gets dramatically enhanced by ≈30 times over the normal PD under 785 nm laser illumination, which is attributed to the largely enhanced localized E-field around BNA arrays at 785 nm wavelength. Under 532 and 633 nm laser illuminations, the normal PD demonstrates comparatively higher responsivity of 71 and 31 mA W^{-1} as compared to 785 nm illuminations due to a larger intrinsic absorption of perovskite in the visible region. However, for plasmonic PD, it has weaker improvements of 33.8% (532 nm) and 58.1% (633 nm) due to a weak enhancement of E-field at 532 and 633 nm. Notice that, the enhancement of E-field at 633 nm is a little higher than that at 532 nm, so the plasmonic EF of the responsivity in plasmonic PD for 633 nm (58.1%) is larger than 532 nm (33.8%). However, the responsivity of PDs at 532 nm

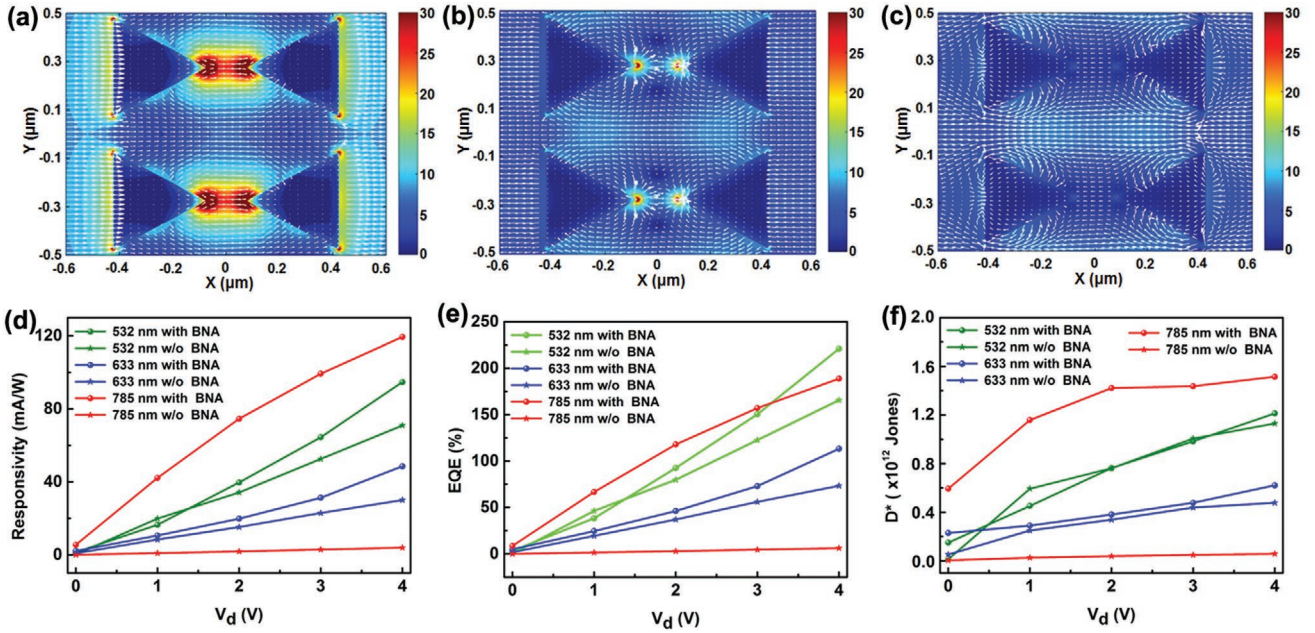

Figure 6. a–c) E-field distribution ($|E|^2/|E_0|^2$) of BNA arrays in *x*-*y* plane under 785, 633, and 532 nm excitation. d–f) The comparison of responsivity, *D**, and EQE of plasmonic (with BNA) and normal (w/o BNA) PDs under 532 (green curve), 633 (blue curve), and 785 nm (red curve) laser illumination with same intensity (11 mW cm^{-2}).

is still larger than 633 nm due to a larger intrinsic absorption of perovskite at 532 nm and a weak E-field enhancement at 633 nm.

Furthermore, comparative demonstrations of *D** and EQE of perovskite PD under 532, 633, and 785 nm laser illuminations at a given intensity of 11 mW cm^{-2} are shown in Figure 6e,f, respectively. Similar to the responsivity, the *D** and EQE of both types of perovskite PDs also increase with an increase in the applied bias voltage, and the plasmonic PD shows a strong plasmonic enhancement for 785 nm as compared to 633 and 532 nm laser illuminations, which is attributed to a large plasmonic enhancement of E-field around BNA arrays under 785 nm excitation. The photoelectric performance of above perovskite PDs under different laser illumination wavelengths are summarized in **Table 1**. These results confirm that the integration of plasmonic BNA arrays in perovskite PD brought its NIR sensitivity level close to the visible, even though the active material has comparatively negligible intrinsic absorption in NIR, realizing broadband photodetection of perovskite PD from visible to NIR spectral range.

2.6. Switching Speed, Time Response, and Stability of Plasmonic Perovskite PD

The switching speed of a PD is a determinant parameter that shows its time response to detect an incident light signal and time to prepare itself to detect next optical event. Generally, it is expressed as "ON" and "OFF" or "recovery" times. The photoswitching, "ON" and "OFF", characteristics of plasmonic and normal PDs under a chopped laser illumination at 785 nm (10.17 mW cm^{-2}, 1 V) are shown in **Figure 7**a. In the dark, the plasmonic PD exhibits a small dark current of few pA. However, when illumination is "turned on," the photocurrent rapidly reached to a level of hundreds of nA, and then drastically decreases to the initial value when illumination is "turned off." An obvious and reproducible photocurrent switching characteristic is observed. The rise and decay portions of one photoswitching cycle are curve fitted by following equations

$$I(t) = I_0 \exp\left(-\frac{t}{\tau_{res}}\right) - I_0 \tag{7a}$$

Table 1. The performance comparison of plasmonic (with BNA) and normal (w/o BNA) PDs.

Device	*R* [mA W^{-1}]	*D** × 10^{12} [Jones]	EQE [%]	Enhancement factor [%]	Wavelength [nm]
with BNA	119.4	1.5	188.8	2962	785
	48.5	0.62	113.3	58	633
	94.7	1.2	220.9	33	532
w/o BNA	3.9	0.058	6.2	–	785
	30.7	0.44	73.4	–	633
	70.9	1.13	165.5	–	532

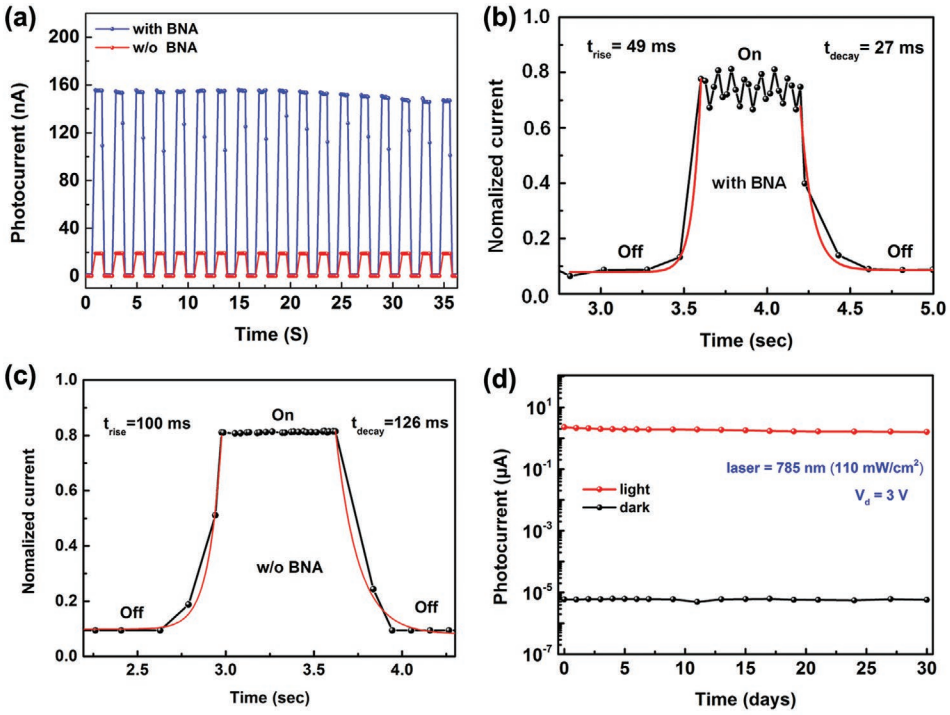

Figure 7. a) The reproducible photocurrent–time (I–t) curves of the plasmonic (with BNA) and normal (w/o BNA) PDs under 785 nm laser illumination (10.17 mW cm^{-2}, 1 V). Dark time: 1 s; illumination time: 1 s. b,c) The photoresponse for rise and decay time of plasmonic (with BNA) and normal (w/o BNA) PDs under 785 nm laser illumination. d) Stabilities in I_p and I_d of the plasmonic perovskite PD during 30 d with 785 nm laser illumination (110 mW cm^{-2}, 3 V).

$$I(t) = I_0 - I_0 \exp\left(-\frac{t}{\tau_{rec}}\right) \quad (7b)$$

where I_0 is the value of current when illumination is in turned on/turned off states, and τ_{res} and τ_{rec} are response and recovery times of the PD.[68] The fitted values of response (rise) and recovery (decay) times are ≈49 and ≈27 ms for plasmonic PD (Figure 7b), ≈100 and ≈126 ms for normal PD (Figure 7c), respectively. The plasmonic PD shows improved and faster response times as compared to the normal PD, which indicates that the BNA-based plasmonic PD can function as a good light switch for the detection of NIR signal.

The stability of perovskite-based devices is a major challenge for their practical implementation and commercialization. As shown in Figure 7d, the BNA-based plasmonic perovskite PD exhibits a stable photoelectric property for over 30 d under 785 nm laser illumination at a bias voltage of 3 V in a nitrogen environment (21 °C average temperature and 10–12% of relative humidity). The I_p and I_d of the plasmonic PD are quite stable and the variation of I_p and I_d is <3% during the test period of 30 d, which suggests the excellent photostability of the plasmonic perovskite PD.[29] The I–V logarithm curves of plasmonic PD at light and dark under 785 nm laser illumination (110 mW cm^{-2}, 3 V) for 30 d are shown in Figure S12 (Supporting Information). All the above data exhibit the outstanding performances of plasmonic perovskite PD, and the device is expected to have a great potential for high-sensitive optical detection and imaging in the infrared. The summary of the state-of-the-art researches of perovskite PD performance is listed in Table S1 (Supporting Information).

3. Conclusion

In conclusion, we theoretically designed and experimentally fabricated a plasmonic BNA array substrate to improve the performance of perovskite ($(Cs_{0.06}FA_{0.79}MA_{0.15})Pb(I_{0.85}Br_{0.15})_3$) PD in NIR spectral region. The plasmonic PD demonstrated a record enhancement factor of 2962% in the photoresponsivity over the normal PD under 785 nm laser illumination, where the intrinsic absorption of the used perovskite active material is very weak. Simultaneously, the plasmonic PD has a D^* value of the order of 10^{12} Jones with EQE as high as 188.8%, more than 30 times over the normal PD, in the detection of NIR light signal under 785 nm laser illumination. The huge improvement in the performance of plasmonic perovskite PD in NIR is due to the large E-field enhancement through LSPR coupling of BNA arrays substrate with incident optical radiation, as confirmed by FDTD simulation. The plasmonic effect on the performance of perovskite PD was also tested for 633 and 532 nm laser illumination wavelengths where the used perovskite material has comparatively higher intrinsic absorption while plasmonic BNA system has weaker E-field enhancement. All the parameters from plasmonic perovskite PD, including responsivity, D^*, and EQE in NIR (785 nm), are comparable to those in visible (532 and 633 nm), even though the intrinsic absorption of perovskite in NIR is negligible as compared to in visible. The plasmonic PD was tested for its photostability for 30 d and demonstrated a strong stability under NIR radiation. Moreover, a large signal-to-background (light/dark) ratio of the order of 10^5, demonstrated by the plasmonic perovskite

PD under 785 nm laser illumination, exhibits its potential applications in the detection of weak or single-photon optical signal. The present study shows that an intelligent design of a plasmonic system can tremendously improve the performance of a perovskite photodetector and extend its spectral bandwidth beyond the perovskite band-edge wavelength. This approach can be widely used in the field of photoelectric and photovoltaic devices for other perovskite materials to improve their broadband light harvesting ability.

4. Experimental Section

Chemicals: Formamidine acetate (99%), lead bromide ($PbBr_2$) (99%), methylamine solution (40% aqueous solution), dimethyl formamide (DMF) (99.5%), and dimethyl sulfoxide (DMSO) (99.5%) were purchased from Aladdin. Cesium iodide (CsI) (99.99%) and lead iodide (PbI_2) (99.99%) were purchased from Xi'an Polymer Light Technology Crop. Hydrobromic acid (HBr) (40% aqueous solution), hydroiodic acid (HI) (55% aqueous solution), ethanol absolute, and diethyl ether were purchased from Sinopharm Chemical Reagent Co, Ltd. All the chemicals were not further purified. Methylammonium bromide (MABr) and formamidinium iodide (FAI) were synthesized by the authors (see Section S15, Supporting Information).

Plasmonic Perovskite PD Fabrication: The plasmonic substrate was firstly fabricated as follows. 20 nm of titanium (Ti) and 50 nm of gold (Au) film were deposited on the surface of Si/SiO_2 wafer (300 nm of SiO_2 on the top of a silicon wafer) by High Vacuum Resistance Evaporation Coating System. 20 nm of SiO_2 spacer layer was deposited on the surface of Au film by plasma enhanced chemical vapor deposition (PECVD) system (Oxford Instruments System 100 PECVD). The photoresist was spin-coated on the surface of SiO_2 spacer layer and patterned using electron-beam lithography (EBL) system (Raith 150 EBL). 10 nm of Ti and 100 nm of Au film were deposited on the surface of photoresist which was developed. The lift-off process was used to fabricate the structure. Next, the perovskite precursor solution was prepared by dissolving PbI_2 (2.766 g), FAI (0.943 g), MABr (0.117 g), and $PbBr_2$ (0.385 g) in the mixture of DMF (4 mL) and DMSO (1 mL) followed by adding 0.25 mL of CsI solution (1.5 M in DMSO).[13,49] Before device fabrication, 10 nm of SiO_2 dielectric layer was deposited on the surface of BNA substrate by PECVD. Then, the precursor perovskite solution was spin-coated on the plasmonic BNA array substrate in a nitrogen-filled glove box at 2000 and 3500 rpm for 15 and 35 s, respectively. And 80 µL of chlorobenzene was poured onto the substrate after 30 s, perovskite film was achieved by thermal annealing at 100 °C for 1.5 h. Finally, the Au S/D electrodes with 80 nm thickness were thermal evaporated on the top of the device via using masks.

Characterization: The UV–vis spectral measurements were carried out using a Cary 5000 UV–vis–NIR spectrometer (Agilent). PL measurements were conducted on Cary Eclipse spectrometer. The thicknesses of plasmonic BNA arrays were measured by a Dimension Icon (Bruker) AFM equipment. XRD spectra were collected using a Bruker D8 FOCUS operated in air at room temperature. SEM and EDS analyses were carried out by the scanning electron microscope (Hitachi S-4800 FESEM and Phenom ProX). XPS data were carried out using X-ray photoelectron spectroscopy (Thermo escalab 250Xi). *I–V* measurements were performed at room temperature using a Keithley 4200A Semiconductor Parametric Analyzer (Tektronix) and a C-100 probe station from TPSi Company. For photoresponsive property measurements, the 532, 633, and 785 nm laser were utilized as laser illumination source for PD measurements. The exposure time of sample was precisely controlled by an optical shutter (VS25S2TO, UNIBLITZ) with a diameter of 2.5 mm.

FDTD Simulations: For the simulations, FDTD method based on Yee's algorithms was employed. In the FDTD method, Maxwell's equations are discretized in both time and space, and central-difference approximation is used. A commercial FDTD package known as Lumerical solutions (Lumerical Inc.) was used to calculate spectral response and E-field distribution of BNA arrays. Perfectly matched layers were used to absorb the scattered radiation in *z*-directions, and periodic boundary conditions were used to perform periodic array in *x*- and *y*-directions. The models are illuminated with a p-polarized plane wave which propagates along *z*-axis and polarizes along *x*-axis from the top of the BNA arrays. Two detector boxes were placed to measure the distribution ($|E_x|$ and $|E_z|$) of E-field. Figure S13 (Supporting Information) gives the schematic of the setting in FDTD simulation as introduced above. An ultrafine mesh size (1 nm) was used in all the simulations, and the simulation time was 1000 fs. The refractive index of $n_{sup} = 1.0$ was chosen for air to generate an asymmetric environment. The optical constants of Au, Ti, SiO_2, and Si were taken from Palik.[69]

Supporting Information

Supporting Information is available from the Wiley Online Library or from the author.

Acknowledgements

This work was supported by the National Key Research and Development Program of China (2018YFB1107202, 2017YFB1104700), National Natural Science Foundation of China (91750205, 61774155, 11774340), K. C. Wong Education Foundation (GJTD-2018-08), Scientific Research Project of the Chinese Academy of Sciences (QYZDB-SSW-SYS038), the Open Project of State Key Laboratory of Supramolecular Structure and Materials (sklssm2019034), and the Bill and Melinda Gates Foundation (OPP1157723).

Conflict of Interest

The authors declare no conflict of interest.

Keywords

bowtie nanoantenna arrays, localized surface plasmon resonance, near infrared, perovskite photodetectors

Received: March 4, 2020
Revised: April 9, 2020
Published online: May 14, 2020

[1] S. D. Stranks, H. J. Snaith, *Nat. Nanotechnol.* **2015**, *10*, 391.
[2] Y. Dong, Y. Zou, J. Song, X. Song, H. Zeng, *J. Mater. Chem. C* **2017**, *5*, 11369.
[3] L. Gu, Z. Fan, *Light: Sci. Appl.* **2017**, *6*, e17090.
[4] C. Wehrenfennig, G. E. Eperon, M. B. Johnston, H. J. Snaith, L. M. Herz, *Adv. Mater.* **2014**, *26*, 1584.
[5] Z. Shi, J. Guo, Y. Chen, Q. Li, Y. Pan, H. Zhang, Y. Xia, W. Huang, *Adv. Mater.* **2017**, *29*, 1605005.
[6] Y. Zhao, C. Li, L. Shen, *InfoMat* **2019**, *1*, 164.
[7] S. D. Stranks, G. E. Eperon, G. Grancini, C. Menelaou, M. J. P. Alcocer, T. Leijtens, L. M. Herz, A. Petrozza, H. J. Snaith, *Science* **2013**, *342*, 341.
[8] W. Hu, H. Cong, W. Huang, Y. Huang, L. Chen, A. Pan, C. Xue, *Light: Sci. Appl.* **2019**, *8*, 106.
[9] G. E. Eperon, T. Leijtens, K. A. Bush, R. Prasanna, T. Green, J. T. W. Wang, D. P. McMeekin, G. Volonakis, R. L. Milot, R. May,

A. Palmstrom, D. J. Slotcavage, R. A. Belisle, J. B. Patel, E. S. Parrott, R. J. Sutton, W. Ma, F. Moghadam, B. Conings, A. Babayigit, H. G. Boyen, S. Bent, F. Giustino, L. M. Herz, M. B. Johnston, M. D. McGehee, H. J. Snaith, *Science* **2016**, *354*, 861.
[10] L. Shen, Y. Fang, D. Wang, Y. Bai, Y. Deng, M. Wang, Y. Lu, J. Huang, *Adv. Mater.* **2016**, *28*, 10794.
[11] A. G. Boldyreva, A. F. Akbulatov, S. A. Tsarev, S. Y. Luchkin, I. S. Zhidkov, E. Z. Kurmaev, K. J. Stevenson, V. G. Petrov, P. A. Troshin, *J. Phys. Chem. Lett.* **2019**, *10*, 813.
[12] C. Xie, P. You, Z. Liu, L. Li, F. Yan, *Light: Sci. Appl.* **2017**, *6*, e17023.
[13] M. Abdi-Jalebi, Z. Andaji-Garmaroudi, S. Cacovich, C. Stavrakas, B. Philippe, J. M. Richter, M. Alsari, E. P. Booker, E. M. Hutter, A. J. Pearson, S. Lilliu, T. J. Savenije, H. Rensmo, G. Divitini, C. Ducati, R. H. Friend, S. D. Stranks, *Nature* **2018**, *555*, 497.
[14] H. Syed, W. Kong, V. Mottamchetty, K. J. Lee, W. Yu, V. R. Soma, J. Yang, C. Guo, *Adv. Opt. Mater.* **2020**, *8*, 1901766.
[15] M. Saliba, T. Matsui, J.-Y. Seo, K. Domanski, J.-P. Correa-Baena, M. K. Nazeeruddin, S. M. Zakeeruddin, W. Tress, A. Abate, A. Hagfeldt, M. Grätzel, *Energy Environ. Sci.* **2016**, *9*, 1989.
[16] X. Xu, C. C. Chueh, P. Jing, Z. Yang, X. Shi, T. Zhao, L. Y. Lin, A. K. Y. Jen, *Adv. Funct. Mater.* **2017**, *27*, 1701053.
[17] W. Wang, D. Zhao, F. Zhang, L. Li, M. Du, C. Wang, Y. Yu, Q. Huang, M. Zhang, L. Li, J. Miao, Z. Lou, G. Shen, Y. Fang, Y. Yan, *Adv. Funct. Mater.* **2017**, *27*, 1703953.
[18] Y. Wu, X. Li, Y. Wei, Y. Gu, H. Zeng, *Nanoscale* **2018**, *10*, 359.
[19] H. Wang, D. H. Kim, *Chem. Soc. Rev.* **2017**, *46*, 5204.
[20] S. K. Pathak, A. Abate, P. Ruckdeschel, B. Roose, K. C. Gödel, Y. Vaynzof, A. Santhala, S. I. Watanabe, D. J. Hollman, N. Noel, A. Sepe, U. Wiesner, R. Friend, H. J. Snaith, U. Steiner, *Adv. Funct. Mater.* **2014**, *24*, 6046.
[21] Z. Yang, A. Rajagopal, C. C. Chueh, S. B. Jo, B. Liu, T. Zhao, A. K. Y. Jen, *Adv. Mater.* **2016**, *28*, 8990.
[22] J. Zhang, M. ElKabbash, R. Wei, S. C. Singh, B. Lam, C. Guo, *Light: Sci. Appl.* **2019**, *8*, 53.
[23] P. Yang, J. Zheng, Y. Xu, Q. Zhang, L. Jiang, *Adv. Mater.* **2016**, *28*, 10508.
[24] R. H. Siddique, J. Mertens, H. Hölscher, S. Vignolini, *Light: Sci. Appl.* **2017**, *6*, e17015.
[25] C. Yao, S. C. Singh, M. ElKabbash, J. Zhang, H. Lu, C. Guo, *Opt. Lett.* **2019**, *44*, 1654.
[26] D. Gao, W. Ding, M. Nieto-Vesperinas, X. Ding, M. Rahman, T. Zhang, C. Lim, C. W. Qiu, *Light: Sci. Appl.* **2017**, *6*, e17039.
[27] A. Dorodnyy, Y. Salamin, P. Ma, J. V. Plestina, N. Lassaline, D. Mikulik, P. Romero-Gomez, A. F. Morral, J. Leuthold, *IEEE J. Sel. Top. Quantum Electron.* **2018**, *24*, 1.
[28] B. Du, W. Yang, Q. Jiang, H. Shan, D. Luo, B. Li, W. Tang, F. Lin, B. Shen, Q. Gong, X. Zhu, R. Zhu, Z. Fang, *Adv. Opt. Mater.* **2018**, *6*, 1701271.
[29] Y. Dong, Y. Gu, Y. Zou, J. Song, L. Xu, J. Li, J. Xue, X. Li, H. Zeng, *Small* **2016**, *12*, 5622.
[30] Z. Sun, L. Aigouy, Z. Chen, *Nanoscale* **2016**, *8*, 7377.
[31] R. T. Ginting, S. Kaur, D. K. Lim, J. M. Kim, J. H. Lee, S. H. Lee, J. W. Kang, *ACS Appl. Mater. Interfaces* **2017**, *9*, 36111.
[32] Z. Lu, X. Pan, Y. Ma, Y. Li, L. Zheng, D. Zhang, Q. Xu, Z. Chen, S. Wang, B. Qu, F. Liu, Y. Huang, L. Xiao, Q. Gong, *RSC Adv.* **2015**, *5*, 11175.
[33] J. Cui, C. Chen, J. Han, K. Cao, W. Zhang, Y. Shen, M. Wang, *Adv. Sci.* **2016**, *3*, 1500312.
[34] K. Ueno, T. Oshikiri, Q. Sun, X. Shi, H. Misawa, *Chem. Rev.* **2018**, *118*, 2955.
[35] S. K. Chamoli, S. Singh, C. Guo, *IEEE Sens. J.* **2020**, *20*, 4628.
[36] D. Etezadi, J. B. Warner, F. S. Ruggeri, G. Dietler, H. A. Lashuel, H. Altug, *Light: Sci. Appl.* **2017**, *6*, e17029.
[37] Y. H. Jang, Y. J. Jang, S. Kim, L. N. Quan, K. Chung, D. H. Kim, *Chem. Rev.* **2016**, *116*, 14982.
[38] K. Y. Nie, J. Li, X. Chen, Y. Xu, X. Tu, F. F. Ren, Q. Du, L. Fu, L. Kang, K. Tang, S. Gu, R. Zhang, P. Wu, Y. Zheng, H. H. Tan, C. Jagadish, J. Ye, *Sci. Rep.* **2017**, *7*, 7503.
[39] H. Chen, A. M. Bhuiya, R. Liu, D. M. Wasserman, K. C. Toussaint, *J. Phys. Chem. C* **2014**, *118*, 20553.
[40] B. Lee, J. Park, G. H. Han, H. S. Ee, C. H. Naylor, W. Liu, A. T. Johnson, R. Agarwal, *Nano Lett.* **2015**, *15*, 3646.
[41] K. Nie, X. Tu, J. Li, X. Chen, F. F. Ren, G. Zhang, L. Kang, S. Gu, R. Zhang, P. Wu, *ACS Nano* **2018**, *12*, 7327.
[42] A. Kinkhabwala, Z. Yu, S. Fan, Y. Avlasevich, K. Müllen, W. E. Moerner, *Nat. Photonics* **2009**, *3*, 654.
[43] J. Y. Suh, C. H. Kim, W. Zhou, M. D. Huntington, D. T. Co, M. R. Wasielewski, T. W. Odom, *Nano Lett.* **2012**, *12*, 5769.
[44] T. Wang, P. Li, D. N. Chigrin, A. J. Giles, F. J. Bezares, O. J. Glembocki, J. D. Caldwell, T. Taubner, *ACS Photonics* **2017**, *4*, 1753.
[45] Y. Zhao, F. Yun, Y. Huang, S. Wang, L. Feng, Y. Li, M. Guo, W. Ding, Y. Zhang, *Sci. Rep.* **2017**, *7*, 41966.
[46] F. Mokhtari-Koushyar, E. Heidari, H. Dalir, C. J. Chung, X. Xu, V. J. Sorger, R. T. Chen, *J. Lightwave Technol.* **2018**, *36*, 3418.
[47] H. Guo, T. P. Meyreth, T. Zentgraf, N. Liu, L. Fu, H. Schweizer, H. Giessen, *Opt. Express* **2008**, *16*, 7756.
[48] J. Cesario, R. Quidant, G. Badenes, S. Enoch, *Opt. Lett.* **2005**, *30*, 3404.
[49] L. Lin, Y. Zheng, *Sci. Rep.* **2015**, *5*, 14788.
[50] B. Wang, S. C. Singh, H. Lu, C. Guo, *Plasmonics* **2019**, https://doi.org/10.1007/s11468-019-01071-z.
[51] B. Wang, C. Zhao, H. Lu, T. Zou, S. C. Singh, Z. Yu, C. Yao, X. Zhen, J. Xing, Y. Zou, C. Tong, W. Yu, B. Zhao, C. Guo, *Photonics Res.* **2020**, *8*, 548.
[52] B. Liu, R. R. Gutha, B. Kattel, M. Alamri, M. Gong, S. M. Sadeghi, W. L. Chan, J. Z. Wu, *ACS Appl. Mater. Interfaces* **2019**, *11*, 32301.
[53] S. M. Sadeghi, W. J. Wing, R. R. Gutha, J. S. Wilt, J. Z. Wu, *Nanoscale* **2018**, *10*, 4825.
[54] M. Abdi-Jalebi, M. I. Dar, S. P. Senanayak, A. Sadhanala, Z. Andaji-Garmaroudi, L. M. Pazos-Outón, J. M. Richter, A. J. Pearson, H. Sirringhaus, M. Grätzel, R. H. Friend, *Sci. Adv.* **2019**, *5*, eaav2012.
[55] Y. Wang, X. Zhou, C. Liang, P. Li, X. Hu, Q. Cai, Y. Zhang, F. Li, M. Li, Y. Song, *Adv. Electron. Mater.* **2017**, *3*, 1700169.
[56] D. Li, D. Zhou, W. Xu, X Chen, G. Pan, X. Zhou, N. Ding, H. Song, *Adv. Funct. Mater.* **2018**, *28*, 1804429.
[57] C. Li, H. Wang, F. Wang, T. Li, M. Xu, H. Wang, Z. Wang, X. Zhan, W. Hu, L. Shen, *Light: Sci. Appl.* **2020**, *9*, 31.
[58] J. R. Lakowicz, *Principles of Fluorescence Spectroscopy*, Springer, Berlin **2006**.
[59] W. Zhang, M. Saliba, S. D. Stranks, Y Sun, X Shi, U. Wiesner, H. J. Snaith, *Nano Lett.* **2013**, *13*, 4505.
[60] C. Zhang, Q. Luo, J. Shi, L. Yue, Z. Wang, X. Chena, S. Huang, *Nanoscale* **2017**, *9*, 2852.
[61] H. F. Zarick, A. Boulesbaa, A. A. Puretzky, E. M. Talbert, Z. R. DeBra, N. Soetan, D. B. Geohegan, R. Bardhan, *Nanoscale* **2017**, *9*, 1475.
[62] N. Li, W. Lan, Y. S. Lau, L. Cai, A. A. Syed, F. Zhu, *J. Mater. Chem. C* **2019**, *7*, 9573.
[63] L. Dou, Y. Yang, J. You, Z. Hong, W. H. Chang, G. Li, Y. Yang, *Nat. Commun.* **2014**, *5*, 5404.
[64] C. Li, J. Lu, Y. Zhao, L. Sun, G. Wang, Y. Ma, S. Zhang, J. Zhou, L. Shen, W. Huang, *Small* **2019**, *15*, 1903599.
[65] Z. Y. Peng, J. L. Xu, J. Y. Zhang, X. Gao, S. D. Wang, *Adv. Mater. Interfaces* **2018**, *5*, 1800505.
[66] Y. Liu, Y. Zhang, Z. Yang, J. Feng, Z. Xu, Q. Li, M. Hu, H. Ye, X. Zhang, M. Liu, K. Zhao, S. Liu, *Mater. Today* **2019**, *22*, 67.
[67] X. Gong, M. Tong, Y. Xia, W. Cai, J. S. Moon, Y. Cao, G. Yu, C. L. Shieh, B. Nilsson, A. J. Heeger, *Science* **2009**, *325*, 1665.
[68] S. C. Singh, Y. Peng, J. Rutledge, C. Guo, *ACS Appl. Electron. Mater.* **2019**, *1*, 1169.
[69] E. D. Palik, *Handbook of Optical Constants of Solids II*, Academic, Orlando, FL **1991**.